Turbulent Couette-Poiseuille flow with zero wall shear

Kun Yang[1], Lihao Zhao [1,2,*], Helge I. Andersson[1]

[1]Department of Energy and Process Engineering, Norwegian University of Science and Technology,
7491 Trondheim, Norway

[2]Department of Engineering Mechanics, Tsinghua University, 10084 Beijing, China

Abstract

A particular pressure-driven flow in a plane channel is considered, in which one of the walls moves with a constant speed that makes the mean shear rate and the friction at the moving wall vanish. The Reynolds number considered based on the friction velocity at the stationary wall ($u_{\tau,S}$) and half the channel height (h) is $Re_{\tau,S} = 180$. The resulting mean velocity increases monotonically from the stationary to the moving wall and exhibits a substantial logarithmic region. Conventional near-wall streaks are observed only near the stationary wall, whereas the turbulence in the vicinity of the shear-free moving wall is qualitatively different from typical near-wall turbulence. Large-scale-structures (LSS) dominate in the center region and their spanwise spacing increases almost linearly from about 2.3 to 4.2 channel half-heights at this $Re_{\tau,S}$. The presence of LSS adds to the transport of turbulent kinetic energy from the core region towards the moving wall where the energy production is negligible. Energy is supplied to this particular flow only by the driving pressure gradient and the wall motion enhances this energy input from to the mean flow. About half of the supplied mechanical energy is directly lost by viscous dissipation whereas the other half is first converted from mean-flow energy to turbulent kinetic energy and thereafter dissipated.

Keywords: Turbulent flows; Couette-Poiseuille flow; Zero wall shear; Large-scale-structures.

1 Introduction

Wall-bounded turbulent flows have been of great interest due to their vital importance of academic as well as industrial relevance. Extensive experimental studies on wall turbulence have been conducted, and an increasing number of relevant numerical studies have appeared for the past several decades thanks to the advancement in computer technology. These studies cover various flow conditions and over a large range of Reynolds number. In particular, studies on a fully developed channel flow have played an important role in understanding the mechanisms of wall-bounded turbulence in general.

A plane channel flow (also referred to as plane Poiseuille flow) is usually defined as a fluid flow driven by a streamwise pressure gradient between two parallel impermeable walls. A useful database on this type of flow was provided by a widely acknowledged direct numerical simulation (DNS) of Kim et al. (1987) at a Reynolds number of 180 (Re_τ, based on the friction velocity at the wall and the channel half-height). For this flow, the statistically-steady turbulence field is homogenous in the wall-parallel planes, and the mean velocity is non-zero only in the streamwise direction. The wall-normal distribution of the primary statistics, including the mean streamwise velocity and the fluctuations of the velocity components, the pressure and the vorticity are all symmetric with respect to the channel center. The total shear stress, defined as the sum of the viscous shear stress and the turbulent shear stress, follows a linear relation and reaches maximum at the two walls and reduces to zero at the channel center. Organized coherent structures in the form of streamwise streaks flanked by alternating vortical structures are generated near the walls. These vortical

structures associate with the sweep and ejection events of high and low velocity respectively, which closely relate to the conversion of mean flow kinetic energy into turbulence energy and finally viscous dissipation (Wallace et al., 1972; Alfredsson and Johansson, 1984; Robinson, 1991). The scales of these inner-layer structures are relatively small, with a spanwise spacing of about 100 wall units (Kim et al., 1987). The formation mechanism for the organized small-scale streaks has been explained in different ways, and is probably a combined phenomenon rather than having one simple universal explanation (Hamilton et al. 1995; Zhou et al., 1996; Jeong et al., 1997; Waleffe, 2001; Jiménez and Pinelli, 2002). A well-recognized theory is that the near-wall streaks and vortical structures are educed by the high mean shear rate in this region (Rogers and Moin, 1987), whereas for regions where there is small shear (e.g. near the channel center), structures of larger scales are likely to form depending on the Reynolds number. This implies that wall proximity is not necessarily a pre-requisite for the formation of such small-scale coherent streaky structures (Lee et al., 1990; Lam and Banerjee, 1992).

The total shear can be easily controlled by allowing the walls to have a relative velocity. A flow driven by the relative wall velocity instead of a pressure gradient is known as a shear-driving Couette flow. Plane Couette flows have also received much attention in the past decades (see for example, Kuroda et al., 1993, 1995; Bech et al., 1995; Bech and Andersson, 1996; Komminaho et al., 1996; Kawahara and Kida, 2001; Tsukahara et al., 2006; Holstad et al., 2009). It has been shown that the wall-normal profile of the turbulent intensities for a plane Couette flow is symmetric with respect to the center line, and the wall-normal distribution of the total shear stress attains a constant value throughout the entire flow. Compared to turbulent Poiseuille flows, the high- and low-speed structures formed in a turbulent Couette flow have two scales, one small scale similar to that of a channel flow, and one larger scale that extends much longer in both streamwise and spanwise directions. The small-scale structures are the coherent streaks observed near the walls, while the large-scale structures are often found in the channel center. These large-scale structures in a plane Couette flow, since first discovered by Lee and Kim (1991), have been reported in many subsequent studies and received different names (e.g. Tsukahara et al., 2006; Pirozzoli et al., 2011). Here they are referred to as Very-Large-Scale Structures (VLSS). There have been some arguments on whether these VLSS are a result of the periodic boundary condition applied in the DNS (Bech et al., 1995), resulting in several studies examining varying sizes of the computational domain (Bech and Andersson, 1994; Komminaho et al., 1996, Holstad et al., 2006, Tsukahara et al., 2006 and Gai et al. 2015). As a general rule, numerical simulations of plane Couette flows always require a much larger domain size than needed for plane Poiseuille flows to avoid unphysical effects of the periodic boundary condition in the homogeneous directions. Tsukahara et al. (2006) reported the influence of the domain size on the size of the VLSS, and suggested that at least a spanwise length of 8 times the channel height is needed for avoiding the effects of the periodic boundary condition. They also reported the global existence of the VLSS and their influences on the near-wall streaks at $Re_\tau = 52$ and $126-129$.

By imposing both a mean pressure gradient and a relative wall velocity, one can obtain a so-called Couette-Poiseuille flow (CP flow). The CP flow serves as a good media to evaluate the combined effects of the driving pressure gradient and the wall shear stress on the varying scales of the flow structures. For example, by adding a spanwise pressure gradient to a shear-driving Couette flow generated between two parallel planes with relative movement, Holstad et al. (2009) evaluated the effects of the skewed mean flow on the coherent turbulent structures in a three-dimensional turbulent boundary layer. To examine the effects of the mean shear, Kuroda et al. (1993, 1995) performed a DNS study on flows between two walls with a varying shear stress by changing the motion of one wall. They presented a variety of turbulence statistics, but the format of the conference proceedings did not allow for any detailed analysis and interpretation of the results. The computational domain size of Kuroda et al. (1993, 1995) was similar to that used by Kim et al. (1987) in their pioneering Poiseuille flow simulation, and is nowadays generally accepted to be

insufficient for Couette flow simulations (e.g. Bech and Andersson 1994, Komminaho et al. 1996, Tsukahara et al. 2006) as well as for Couette-Poiseuille flows (Pirozzoli et al. 2011). A very recent DNS study of Pirozzoli et al. (2011) using a much larger domain (see Table 1) covered different flows ranging from a pure Poiseuille flow (or a P flow) to a pure Couette flow (or a C flow) at $Re_{\tau,S} = 250$, a Reynolds number based on the friction velocity at the stationary wall. In particular, they pointed out that the specific CP flow with zero mean shear at the moving wall is of special value in evaluating the effects of the total shear. They observed the existence of streaky structures in the near-wall region of both the P flow and the C flow. Structures of larger scale were observed in the center region for the CP flow and the C flow. For the CP flow, Pirozzoli et al. (2011) showed the coexistence of the two scales and the superimposing of the LSS onto the near-wall small-scale structures by way of a two-point amplitude modulation coefficient. In general, there is an enhanced near-wall influence of the outer-layer large-scale structures from P-like to C-like flows. The VLS found for the C flows have a size in the order of the channel height and their center locates at the channel centerline (similar to that reported in other studies on C flow, e.g. Tsukahara et al. 2006), whereas the LSS associated with CP flow have a less influencing range and their center deviates from the channel centerline. Similar large-scale structures have also been detected in turbulent Poiseuille and boundary-layer flows at high Reynolds number (see e.g. Balakumar and Adrian 2007). In hybrid channel flows, i.e. CP flows, the presence of large-scale structures depends on whether the actual flow is C-like or P-like. Since Couette flows are known to have a characteristic length scale that is much longer than those found in P flows at high Reynolds numbers, the intermediate case of a CP flow with zero mean wall shear is believed to exhibit LSS of size somewhere in between pure P flows and pure C flows. It is likely that these differences are associated with the variation of the mean velocity between the two walls. The mean velocity exhibits an inflection point midway between the walls in C flows, and as the flow becomes less and less C-like the inflection point gradually shifts towards the moving wall until it finally vanishes for the CP flow with zero mean shear. Shear-less CP flows were also addressed in recent studies of Coleman and Spalart (2015) at $Re_{\tau,S} = 850$ and Coleman et al. (2016) at $Re_{\tau,S} = 282 \sim 975$, who proposed a linear relation between the mean velocity and the square-root of the normalized wall-normal coordinate near the moving wall.

The present work focuses on a CP flow with zero mean shear at one moving wall at $Re_{\tau,S} = 180$, controlled by a prescribed streamwise pressure gradient and a relative velocity between the two walls. After a brief description of the numerical method and flow validation, the results of the current CP flow are presented in mainly three aspects. Firstly, the primary statistics for the CP flow is discussed. Secondly, the turbulent structures formed in the CP flow are analyzed, and in particular, different scales of the flow structures are evaluated. In this study, the large-scale structures are referred to as LSS (Large-Scale Structures) for the CP flows in order to distinguish with the larger VLSS (Very-Large-Scale Structures) for the Couette flows. Last but not least, the kinetic energy and its internal conversion associated with the present CP flow are considered. Extensive comparison with the turbulent Poiseuille flow database of Kim et al. (1987) is carried out to address the effects of the wall motion.

2   Methodology

2.1   *Governing equations and Numerical methods*

The present study considers incompressible Newtonian turbulent fluid flow between two impermeable parallel planes with a relative velocity. The governing equations for the flow are the incompressible Navier-Stokes equation and the continuity equation, which can be written as (after normalized by the friction velocity at the stationary wall $u_{\tau,S}$ and half the channel height h):

$$\frac{\partial \tilde{u}_i}{\partial t} + u_j \frac{\partial \tilde{u}_i}{\partial x_j} = -\frac{\partial \tilde{p}}{\partial x_i} + \frac{1}{Re_{\tau,\mathrm{S}}} \frac{\partial^2 \tilde{u}_i}{\partial x_j \partial x_j} \qquad 2.1$$

$$\frac{\partial \tilde{u}_i}{\partial x_i} = 0, \qquad 2.2$$

where $\tilde{u}_i$ is the dimensionless instantaneous velocity normalized by $u_{\tau,\mathrm{S}}$, and $\tilde{p}$ is the dimensionless instantaneous pressure normalized by $\rho u_{\tau,\mathrm{S}}^2$, where ρ is the fluid density. The instantaneous velocity $\tilde{u}_i$ can be decomposed into a mean flow and corresponding velocity fluctuations (i.e. $\tilde{u}_x = U+u$, $\tilde{u}_y = V+v$, and $\tilde{u}_z = W+w$ in x-, y- and z-directions, respectively). The mean flow is obtained by averaging in homogenous (x, y) directions and time. The friction Reynolds number based on $u_{\tau,\mathrm{S}}$ is defined as $Re_{\tau,\mathrm{S}} = u_{\tau,\mathrm{S}}h/v$, where v is the fluid kinematic viscosity. In this study $Re_{\tau,\mathrm{S}}$ is set at 180. Based on this $Re_{\tau,\mathrm{S}}$ value, the physical quantities are scaled using $u_{\tau,\mathrm{S}}$ and v to obtain the viscous units, by $u_i^+ = \tilde{u}_i/u_{\tau,\mathrm{S}}$, $x_i^+ = x_i/(v/u_{\tau,\mathrm{S}})$, $t^+ = t/(v/u_{\tau,\mathrm{S}}^2)$, and $p^+ = p/\rho u_{\tau,\mathrm{S}}^2$.

The computational domain is demonstrated in Fig. 1 together with the coordinate system. The size of the current domain is $36h \times 10h \times 2h$ in streamwise (x-), spanwise (y-), and wall-normal (z-) directions, respectively. The bottom wall ($z/h = 0$) is stationary and the top wall at $z/h = 2$ has a relative velocity of $U_{\mathrm{wall}} = 20u_{\tau,\mathrm{S}}$. This particular wall velocity depends on the actual Reynolds number and was determined by a trial-and-error procedure starting from the wall speed of $U_{\mathrm{wall}} = 19.48u_{\tau,\mathrm{S}}$ reported by Kuroda et al. (1993,1995) at $Re_{\tau,\mathrm{S}} = 154$. Here we intentionally decided to consider a flow with $Re_{\tau,\mathrm{S}} = 180$ in order to facilitate direct comparisons with results from the benchmark Poiseuille flow simulation by Kim et al. (1987), since we anticipate close similarities in the near-stationary-wall turbulence between our CP flow case and the canonical Poiseuille flow case. At both walls a no-slip boundary condition is applied. A periodic boundary condition is used in the homogenous xy- directions. A driving pressure gradient corresponding to $Re_{\tau,\mathrm{S}} = 180$ is also added to the present flow. The values of the two controlling parameters, i.e. the relative wall velocity and the pressure gradient, were chosen to achieve a vanishing shear at the moving wall ($|\tau_{\mathrm{M}}/\rho u_{\tau,\mathrm{S}}^2| \approx 0$). Although the mean shear rate and thereby the mean friction is practically zero, the instantaneous shear rate and the instantaneous shear stress at the moving wall fluctuate about an almost zero mean value. For the present CP flow, we were able to obtain a flow field with a statistically low mean value of $|\tau_{\mathrm{M}}/\rho u_{\tau,\mathrm{S}}^2| \approx 3\times10^{-3}$. The friction Reynolds number based on the moving wall friction velocity $u_{\tau,\mathrm{M}}$ becomes $Re_{\tau,\mathrm{M}} \approx 9.8$.

Comparison of the current computational domain with previous studies is given in Table 1. The current domain size is close to but slightly smaller than the one used by Pirozzoli et al. (2011), because they considered also Couette flows, which have even larger-scale structures in the flow (VLSS for C-like flows). Kuroda et al. (1993, 1995) also investigated all flow regimes from P-like flows to C-like flows at a smaller $Re_{\tau,\mathrm{S}}$, with a much smaller domain than the present one. Specifically, our domain is about 2.3 times the streamwise length and about 1.6 times the spanwise width as that of Kuroda's domain. The present domain is also much larger than that of the P flow case of Kim et al. (1987) at the same $Re_{\tau,\mathrm{S}}$, due to the possible formation of the LSS in the current CP flow. For the discretization of the current domain, the number of grid points in the x-, y- and z- directions are 576, 260 and 192, respectively. The mesh resolution in the homogeneous plane (xy plane) is uniform, with $\Delta x^+ = 11.25$ and $\Delta y^+ = 6.93$ (normalized by viscous units). In the wall-normal direction, the grids are non-uniform and are increasingly finer closer to the two walls. The first grid spacing near the wall is $\Delta z^+ = 0.88$ and the largest grid spacing ($\Delta z^+ = 2.86$) is found at the channel center. From Table 1 it is seen that the current grid resolution is similar to that of Kim et al. (1987), and is slightly coarser than that of Pirozzoli et al. (2011). This is because our $Re_{\tau,\mathrm{S}}$ is similar with Kim et al.'s case but lower than Pirozzoli et al.'s case.
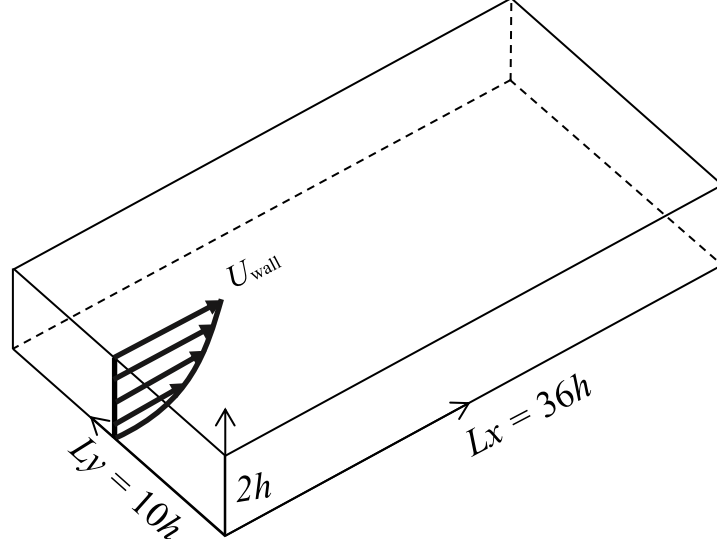
Fig. 1. Sketch of the present computational domain and coordinate system.

Table 1. Comparison of the present computation with previous studies. *Only the cases with the finest mesh at different Reynolds number (Case C3000, C6000a, C12000) of Coleman et al. (2016) are shown in this table.

	$Re_{\tau,S}$	$Re_{\tau,M}$	Domain size $L_x \times L_y \times L_z$	Grid number $n_x \times n_y \times n_z$	Δx^+	Δy^+
Kim et al. (1987)	180	-	$4\pi h \times 2\pi h \times 2h$	192×160×129	11.8	7.1
Kuroda (1993, 1995) CP3	154	17.7	$5\pi h \times 2\pi h \times 2h$	128×128×96	18.9	18.9
Pirozzoli et al. (2011) SL	255	26	$12\pi h \times 4\pi h \times 2h$	1024×512×256	9.4	6.3
Coleman & Spalart (2015)	850	ca. 0	$4\pi h \times 2\pi h \times 2h$	576×576×193	18.5	9.3
Coleman et al. (2016)*	282 520 975	6.9 7.4 23.9	$4\pi h \times 2\pi h \times 2h$	576×432×257 1152×864×385 1152×1536×385	6.2 5.7 10.7	4.1 3.8 4.0
Present DNS CP flow	180	9.8	$36h \times 10h \times 2h$	576×260×192	11.3	6.9

The present DNS code uses a pseudo-spectral method in the homogeneous directions, and a second-order central finite difference method in the wall-normal direction. This method has been used by Gillissen et al. (2007), Mortensen et al. (2008) and Zhao et al. (2013), to which interested readers are referred for more details about the numerical scheme. The code has been well validated against Poiseuille flow cases, but since this is the first time it is used for a CP flow case, a flow validation against a previous study is therefore conducted.

2.2 Flow validation

The calculations were started with a random flow field and allowed to develop in time. The time step for the DNS is $\Delta t = 0.0002 h/u_{\tau,S}$, or 0.036 in viscous units ($\nu/u_{\tau,S}^2$). After the statistically steady turbulent flow field has been established, the simulations were continued in order to collect sufficient independent

samples (122 samples, taken from $t = 53.1h/u_{\tau,S} \sim 65.2h/u_{\tau,S}$) for statistical convergence of the results to be analyzed in this study.

The current zero-mean-shear CP flow field is validated by comparing to the similar flow of the CP3 case of Kuroda et al. (1993, 1995), which also has an almost shear-free moving wall. However note that the friction Reynolds number for the two cases are slightly different (see Table 1). Without losing generality, selected primary statistic quantities will be compared in the following.
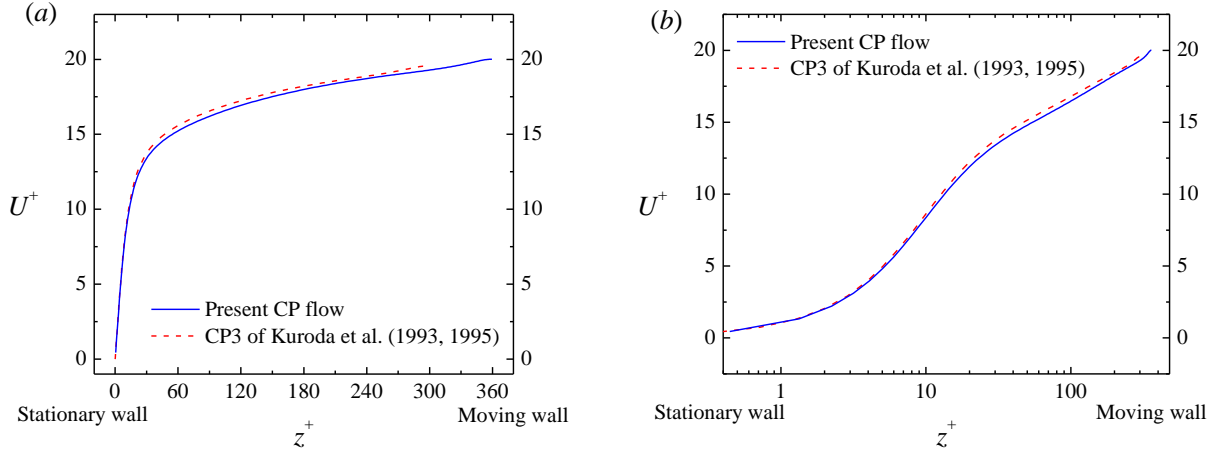
Fig. 2. Normalized mean-velocity profiles compared to case CP3 of Kuroda et al. (1993, 1995). (b) is the semi-log plot of (a).

The wall-normal distribution of the normalized mean streamwise velocity ($U^+ = U/u_{\tau,s}$) of the two cases are compared in Fig. 2. The mean velocity is obtained by averaging in the homogeneous directions and time. The normalization is realized using the wall units at the stationary side, which depends on the $Re_{\tau,S}$ of each case. Therefore, z^+ ranges from 0 to 360 for the current CP case and from 0 to 308 for Kuroda et al. (1993, 1995)'s case. It is obvious from Fig. 2 that the profiles of the two cases overlap well across the whole domain. The distributions of U^+ for both cases have a linear trend in the viscous sublayer and follow a logarithmic relation over a long distance to the upper wall (Fig. 2 (b)). From Fig. 2 (a) we see that both curves are almost flat next to the moving wall, indicating the mean streamwise velocity gradient $dU^+/dz^+ \approx 0$. This gives a zero viscous shear ($\mu dU^+/dz^+$) approaching the moving wall, which is one proof of the total shear stress at the moving wall to be zero, since due to the no-slip boundary condition, the turbulent shear stress $-\rho\overline{uw}$ is also zero at the moving wall. The comparison of the stresses is not presented here for brevity.
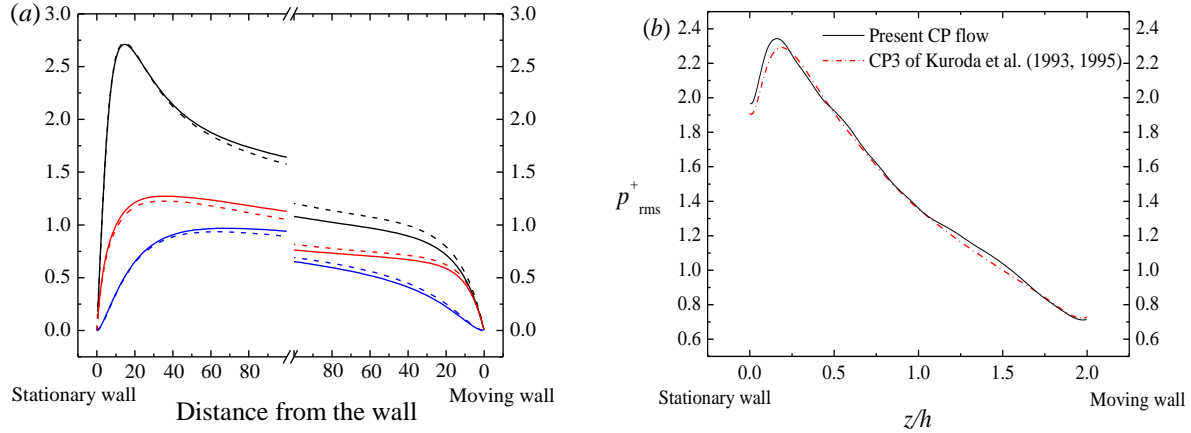
6

Fig. 3. Normalized fluctuating quantities compared to case CP3 of Kuroda et al. (1993, 1995). (a) RMS velocity fluctuations at the normalized distance away from the nearby wall. Solid lines: the present results; dashed lines: Kuroda et al. (1993, 1995)'s results. Black: u^+_{rms}; Red: v^+_{rms}; Blue: w^+_{rms}. (b) Wall-normal distribution of the RMS pressure normalized by the viscous units. Notice that the data for the pressure fluctuations are not included in the papers by Kuroda et al. (1993, 1995) but taken from the database at http://www.thtlab.jp/. Contrary to the distributions of the velocity fluctuations in panel (a), the pressure profile in panel (b) is stretched to extend from wall to wall, i.e. from $z/h = 0$ to 2.

The fluctuating quantities of the two flows are also compared. Fig. 3 (a) shows the comparison of the normalized turbulent intensities (u^+_{rms}, v^+_{rms} and w^+_{rms}) near the two walls. Note that, as mentioned before, the overall wall-normal span of the current CP flow in z^+ is 360 while that of Kuroda's case is 308 due to the different $Re_{\tau,S}$ between the two cases. In Fig. 3 (a), a distance of $100\nu/u_\tau$ (viscous length) away from the neighboring wall is shown as the zoom-in region. Overall good agreement between the two cases is observed, such as the slopes of the curves and the location of the peaks; in particular, better agreement is found near the stationary wall than near the moving wall. Compared to Kuroda's case, all velocity fluctuations from the current CP flow are slightly larger near the stationary wall, while slightly smaller near the moving wall. This difference might be attributed to the difference in $Re_{\tau,S}$. Fig. 3 (b) shows the comparison of the wall-normal distribution of the normalized pressure fluctuation (p^+_{rms}) between the two cases. Again the comparison is satisfactory. The modest shift of the peak of the p^+_{rms} distribution is primarily caused by the usage of the outer scaling z/h rather than inner scaling z^+.
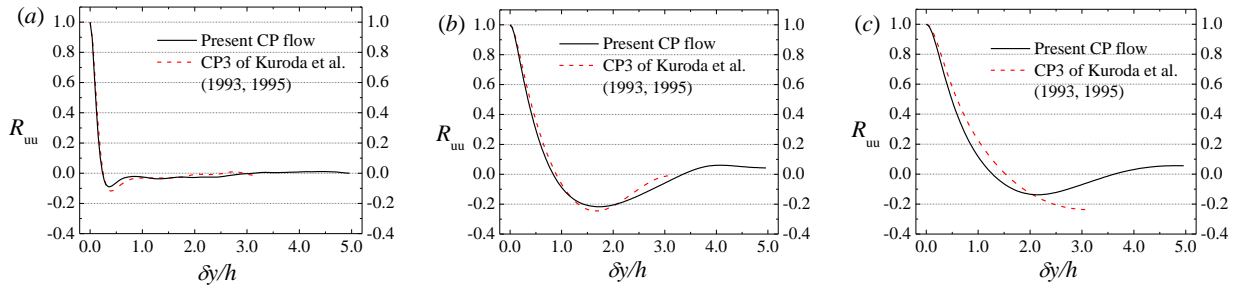

Fig. 4. Spanwise two-point correlation coefficient of streamwise velocity fluctuation (R_{uu}) calculated for wall-parallel planes at selected z/h values. (a) Near the stationary wall at $z/h = 7 \times 10^{-2}$; (b) at the center plane $z/h = 1$ and (c) near the moving wall at $z/h = 1.92$. Comparison between the present CP flow and the CP3 of Kuroda et al. (1993, 1995) in each panel. Data of Kuroda et al. taken from the database at http://www.thtlab.jp/.

In addition to the primary statistical quantities, it is also relevant to study the spatial two-point correlations. As mentioned in many previous studies (e.g. Kim et al.,1987; Kuroda et al., 1993, 1995;

Tsukahara et al., 2006), the streamwise and spanwise two-point correlations coefficients calculated in the homogenous plane can be used to evaluate the sufficiency of the computational domain size. In addition, the spanwise two-point correlation coefficient of the streamwise velocity fluctuation is often used to evaluate the spanwise spacing of the coherent turbulent structures (e.g. streaks). This spanwise two-point correlation coefficient, $R_{uu}(\delta y)$, is defined as

$$R_{uu}(\delta y) = \frac{\overline{u(x, y, z, t)\, u(x, y+\delta y, z, t)}}{u_{rms}(x, y, z, t)\, u_{rms}(x, y+\delta y, z, t)} ,$$

2.3

where u and u_{rms} are respectively the instantaneous streamwise velocity fluctuation and the RMS of the fluctuation, and δy is the spanwise distance between two sampling points.

Fig. 4 shows the comparison of the time-averaged spanwise R_{uu} at selected z/h values. The results from the two studies compare well in Fig. 4 (a) and (b), but not in (c). At z/h near the stationary wall (Fig. 4 (a)), a clear negative minimum value is seen at $\delta y/h \approx 0.3$ for the present CP flow and at $\delta y/h \approx 0.4$ for Kuroda et al.'s case. This yields a similar δy^+_{min} of about 55 for both cases. It is known that the negative peak of spanwise R_{uu} stands for the spacing between the alternating high- and low- streamwise velocity regions, based on which $\lambda^+ = 2\delta y^+_{min}$ is defined as the spacing between a pair of streaks formed near the stationary wall. Therefore, the spanwise spacing λ^+ of the near-stationary-wall coherent streaky structures is 110 for both cases. At the center plane (Fig. 4 (b)), the negative peak is much less prominent than near the stationary wall. Also, the negative minimum value of R_{uu} is now found at $\delta y/h \approx 1.7$ for both cases at this z/h (center plane). This less prominent negative peak is associated with the LSS. Near the moving wall (Fig. 4 (c)), it can be observed that our spanwise length is large enough to accommodate a negative peak of R_{uu}, which is again not as prominent as for the near-wall peak in Fig. 4 (a). However, this negative peak of R_{uu} was not captured by Kuroda et al. (1993, 1995) due to a smaller spanwise width of their domain (see Table 1). By comparing between Fig. 4 (a), (b) and (c) it is concluded that, from the stationary wall to the moving wall, the location of the negative minimum value of R_{uu} migrates to a larger $\delta y/h$, indicating an increasing spanwise spacing between the high- and low-velocity regions, i.e. the structures have a gradually larger spanwise scale. This point will be further explored later. It is also worthwhile noting that, the blunt negative peak in Fig. 4 (c) has a similar $\delta y/h$ station as in a Couette flow at different values of $Re_{\tau,S}$ (Tsukahara et al. 2006 and Avsarkisov et al., 2014).

3 Results

After the flow field has been validated, the results obtained from the current CP flow will now be discussed. First we present the primary flow statistics obtained from 122 flow samples after the flow has reached a fully developed and statistically steady state. Then the flow structures associated with this particular shear-less CP flow are examined. Finally, the kinetic energy and its conversion within the flow field will be analyzed. In the following discussions, we will frequently compare our results with those of the turbulent Poiseuille flow case of Kim et al. (1987) at the same $Re_{\tau,S}$ of 180.

3.1 Primary flow statistics

If the flow has reached a statistically-steady state, the total mean shear stress should follow a linear relation

$$\tau_{total} = -\frac{dP}{dx}(2h - z)$$

3.1

8

which can be obtained by integration of the *x*-component of the Reynolds-averaged Navier-Stokes equation in the wall-normal direction (Tennekes and Lumley, 1972).

Fig. 5 shows the mean viscous stress, mean turbulent stress and mean total stress, all normalized by stationary-wall units. For a better comparison, a referencing straight line is also plotted in Fig. 5 (a). A linear distribution of the total shear stress for the present CP flow is clearly observed, which confirms the statistical steady state of the current CP flow. It also shows that, at the moving wall (at $z^+ = 360$), the mean total shear has a negligible value of $|\tau^+_M| \approx 0.003$, i.e. less than 1%. Fig. 5 (b) shows the comparison between the current CP flow and the Poisuille flow of Kim et al. (1987). Firstly, the most noticeable distinction of the current CP flow from the P flow is the breakdown of symmetry of all the stresses: for the CP flow, the viscous stress and the total stress are the highest at the stationary wall, and all stresses go to zero at the moving wall; on the contrary, for the P flow, all normal stresses have a symmetric distribution with respect to the center plane ($z/h = 1$), where the shear stress is zero. Secondly, it is interesting to compare the two flows in the lower half of the domain ($z/h = 0$ to 1) near the stationary wall. In this region, the viscous stress for the two flows is similar, while the turbulent stress shows a greater difference. The CP flow has a higher turbulent stress near the stationary wall, in particular with a higher and broader peak at $z^+ \approx 38$. After the peak, the slope of the decreasing $-\overline{u^+w^+}$ of the CP flow is half of that of the channel flow.
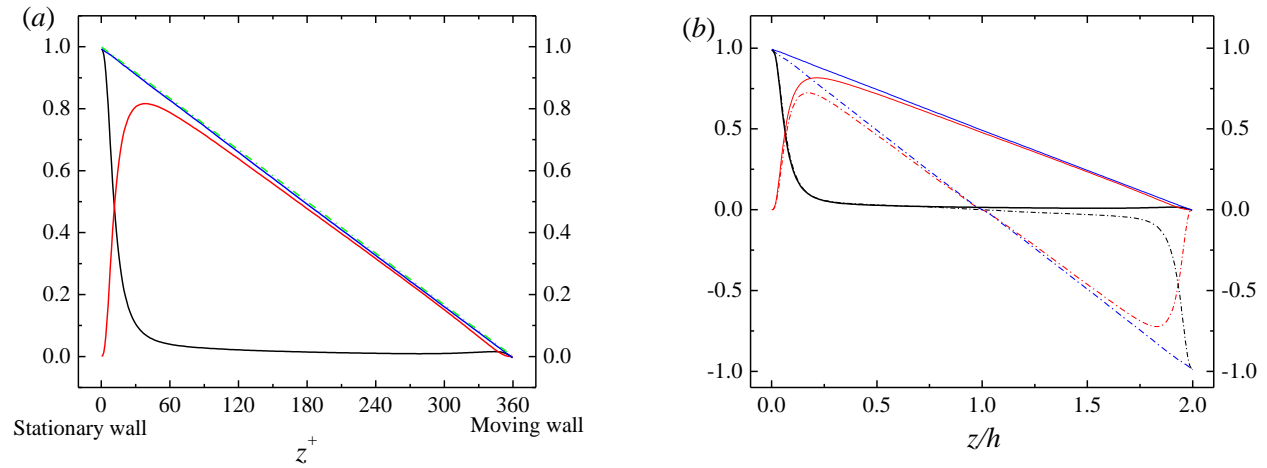

Fig. 5. Mean shear stresses normalized by wall units. (a) Distribution with z^+ for the present CP flow. In both figures, black: dU^+/dz^+; red: $-\overline{u^+w^+}$; blue: τ^+_{total}; green: referencing straight line. (b) Distribution with z/h and compared to the P flow case of Kim et al. (1987). Solid lines: present study; dashed lines: Kim et al. (1987)'s results.
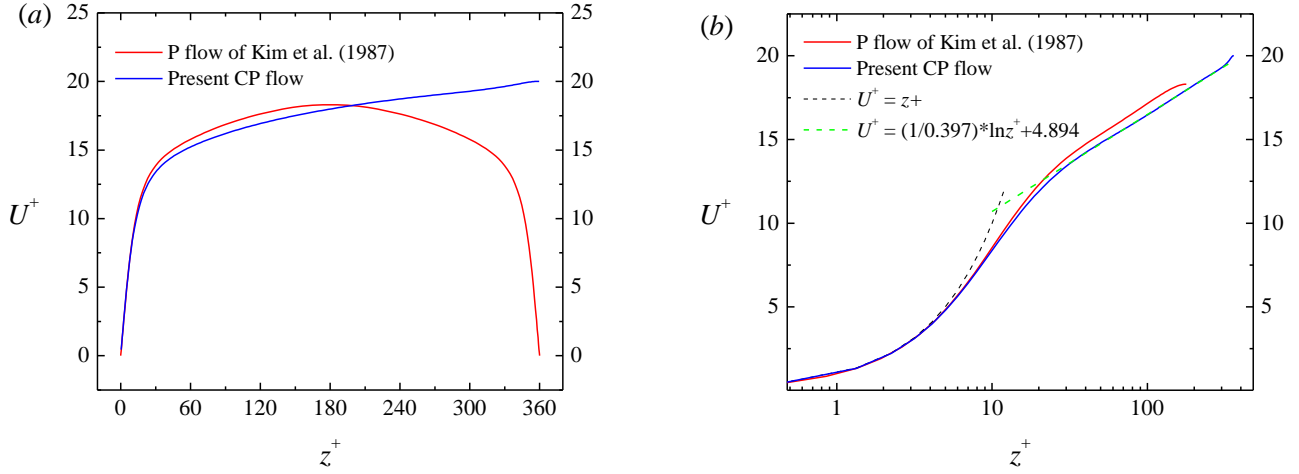
Fig. 6. Wall-normal profile of the normalized mean streamwise velocity compared to Kim et al. (1987). (a) Linear plot and (b) semi-log-scale plot.

The wall-normal distribution of the normalized mean streamwise velocity U^+ from two flows are compared in Fig. 6. As Fig. 6 (a) shows, the current CP flow has a monotonically growing U^+, which reaches a maximum value equaling to the prescribed relative velocity of the wall motion. On the contrary, U^+ of the P flow has a symmetric distribution with its maximum value located at the channel center. Even near the stationary wall, the two curves representing different flows are not exactly overlapping. This is better viewed in the semi-log-scale plot of U^+ in Fig. 6 (b). In the viscous sublayer near the stationary wall, distributions of U^+ from the two flows agree well. The logarithmic relation of U^+ for the CP flow starts after about $z^+ \approx 25$ and lasts until very close to the moving wall. This is a much longer logarithmic region than the P flow case, whose log-region ends before the channel center. It is observed from Fig. 6 (b) that, in the logarithmic sublayer, the current CP flow has a slightly lower U^+ than the P flow, therefore the additive constant B of the log-scale approximation $U^+ = \kappa \ln z^+ + B$ for the CP flow is smaller than that for the P flow. Also, the von Karman constant κ of CP flow from the log-scale approximation is slightly larger than that of the P flow case. A linear curve fitting using 105 sampling points in the logarithmic region of the U^+ curve for the CP flow (blue) in Fig. 6 (b) yields $\kappa = 0.397$ with a small standard error of 0.3% and $B = 4.894$ with a standard error of 1.7%. Note that the value of κ found here is higher than that obtained by Coleman et al. (2016) at higher $Re_{\tau,S}$ values, who found $\kappa \approx 0.36 - 0.37$. Referencing lines of $U^+ = z^+$ and $U^+ = (1/0.397) \times \ln z^+ + 4.894$ are also plotted in Fig. 6 (b). The results of the current CP flow provide useful data for validating the log-scale approximation in general wall-bounded turbulence. The velocity at the center plane is $U^+_c \approx 18.0$ for the CP flow, slightly smaller than $U^+_c \approx 18.3$ for the P flow. Past the center plane, U^+ of the CP flow continues to grow, while U^+ of the P flow starts to decrease due to symmetry. Slightly beyond $z/h = 1$, the increasing U^+ of the CP flow catches up with the decreasing U^+ of the P flow, and becomes increasingly larger than the latter further approaching the moving wall.
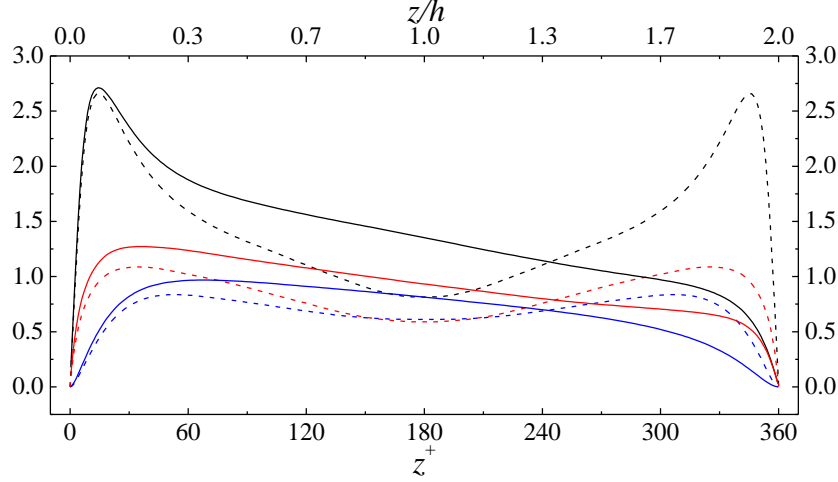
Fig. 7. Wall-normal profile of the normalized velocity fluctuations compared to Kim et al. (1987). Solid lines: the present CP flow results; dashed lines: Kim et al. (1987)'s results. Black: u^+_{rms}; red: v^+_{rms}; blue: w^+_{rms}.

The features of the fluctuating quantities of the CP flow are now considered. Fig. 7 presents the normalized turbulent intensities (u^+_{rms}, v^+_{rms} and w^+_{rms}) and their comparison with the P flow case by Kim et al. (1987)'s results. Firstly, it is seen that the distributions of all the turbulent intensities for CP have an overall decreasing trend from near the stationary wall to the moving wall, and are not symmetric like the P flow case. The magnitudes of the three components are always $u^+_{rms} > v^+_{rms} > w^+_{rms}$ for the two cases, except for the channel flow at the center line, where $u^+_{rms} > v^+_{rms} \approx w^+_{rms}$. All components of the turbulent intensities for the CP flow are higher than the P flow near the stationary wall, leading to a higher turbulent kinetic energy (TKE), as will be discussed more later. For $z^+ < 50$, all components grow quickly, and reach a peak at different z^+ values. Note that the peak magnitudes of the CP flow are slightly higher than those of the P flow, especially for v^+_{rms} and w^+_{rms}. After the peak, all components decrease towards the moving wall. The rate of change before and after the peak follows $u^+_{rms} > v^+_{rms} > w^+_{rms}$. The sharp increasing and decreasing of u^+_{rms} form a distinct peak close to the stationary wall at $z^+ \approx 12$. After this peak, u^+_{rms} decreases sharply up to the station $z^+ \approx 50$ (this is where w^+_{rms} has a maximum value). From this point onwards, all three components decrease at a relatively small rate across a large center region until close to the moving wall. For example, in a range of $z^+ = 100$ to 260, the slopes obtained from curve-fitting for u^+_{rms}, v^+_{rms} and w^+_{rms} are -0.63, -0.42 and -0.31, respectively. The decreasing rates of the CP flow components are smaller than those of the P flow, therefore the turbulent intensities in the center of the CP flow are stronger than in the center of the P flow. Near the moving wall, all components approach zero due to the no-slip and impermeability effects of the wall. The reduction of the turbulent intensities is relatively abrupt like near the stationary wall, especially for u^+_{rms} and v^+_{rms}. The decreasing rates are again in the order of $u^+_{rms} > v^+_{rms} > w^+_{rms}$, however the rate of change for each component at the moving wall is smaller than at the other wall. Compared to the P flow case, near the moving wall the magnitudes of all components are also much smaller and there is no peak of u^+_{rms}, indicating the absence of turbulence regeneration in this region. The values of u^+_{rms}, v^+_{rms} and w^+_{rms} next to the moving wall before they start to decrease (at $z^+ \approx 320$) are close to the values of u^+_{rms}, v^+_{rms} and w^+_{rms} at the center plane of the P flow, which can be contributed to the vanishing shear at both locations.

The wall-normal distribution of the normalized fluctuating pressure (p^+_{rms}) is also compared with the P flow case (figure not shown, refer to Fig. 3 (b) in this paper and Fig. 9 of Kim et al. (1987)). For the CP flow near the stationary wall, p^+_{rms} increases first before it decreases almost linearly approaching the moving wall, forming a peak at $z^+ \approx 30$. In the half domain next to the stationary wall (i.e. $z/h = 0$ to 1), the p^+_{rms}

curves of the two cases are similar in both the trend and the locations of the peaks, but the magnitude of p^+_{rms} for the CP flow case is larger (approximately 20%) than that of the P flow. The symmetry breaks down for the CP flow case and there is no peak of p^+_{rms} near the moving wall for the CP flow.
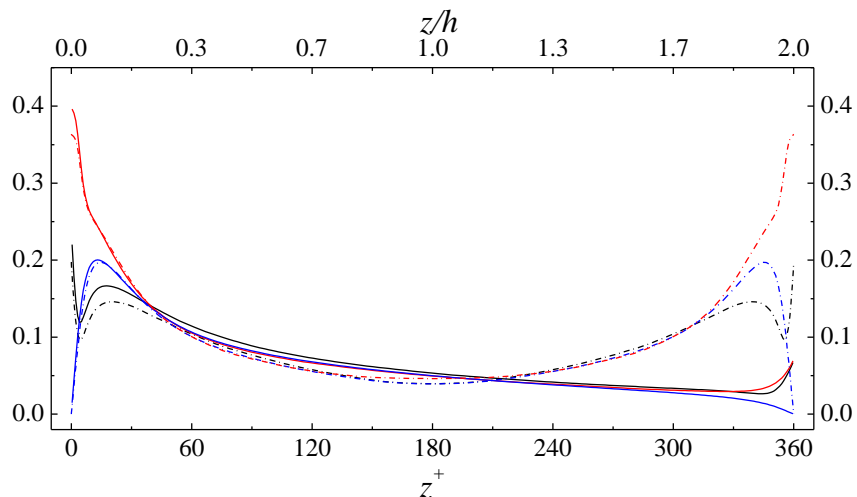

Fig. 8. Wall-normal profile of the normalized vorticity fluctuations compared to Kim et al. (1987). Solid lines: present CP flow results; dashed lines: Kim et al. (1987)'s results. Black: ω^+_x; red: ω^+_y; blue: ω^+_z.

The RMS values of the normalized vorticity fluctuations in three directions are presented in Fig. 8, together with the results from Kim et al. (1987)'s P flow case. It is apparent that the distributions of all three fluctuation components near the stationary wall have a very similar behavior with those of the P flow case. The trend of the all three curves are the same, and in particular, the curves of ω^+_y and ω^+_z from the two cases overlap very well. There is a slight enhancement in the magnitude of ω^+_x for the CP flow, indicating the near-wall streamwise vortices become more powerful in the CP flow due to the imprinting of LSS onto the near-wall small-scale structures. The large value of ω^+_x at the stationary wall is due to the near-wall vorticity induced by the no-slip boundary condition (Kim et al. 1987, Orlandi & Jiménez 1994). The peak of ω^+_x at $z^+ \approx 20$ is associated with the center of the streamwise vortices, and the minimum value in-between the high wall-value and this peak indicates the edge between the near-wall vorticity and the streamwise vortices (Kim et al.,1987). Moving away from the stationary wall and into the channel center, all vorticity components become equal and decrease almost monotonically until close to the moving wall (to about $z^+ \approx 350$), where significant differences between the two flows are observed, caused by the distinct wall conditions. For the CP flow, there is no peak of ω^+_x near the moving wall, which implies the absence of the local streamwise vortices like those formed near the stationary wall. The absence of streamwise vortices and their associated streaky structures near the moving wall is unique in the shear-free CP flow, compared with P-like and C-like flows. Due to the LSS in the channel and the shear-less no-slip boundary condition at the moving wall, ω^+_x and ω^+_y begin to increase and finally reach a similar wall value. The wall-induced vorticities of ω^+_x and ω^+_y near the moving wall span larger than the stationary wall (approx. 10 wall units vs 5 wall units), indicating a larger region of anisotropy than the latter, but their values at the moving wall are much smaller than at the stationary wall. The wall-normal vorticity component ω^+_z is the only component that does not increase at the moving wall, and it goes to zero at both walls due to the no-slip conditions.

12

3.2 Turbulent flow structures

In this section we will discuss the specific flow structures generated in this particular shear-less CP flow, with a focus on the different scales of structures. First flow visualization is provided to distinguish the prominent scales, then more information regarding the primary scales is obtained by investigating the spanwise two-point correlation coefficient of the streamwise velocity fluctuations, as mentioned in conjunction with Fig. 4.
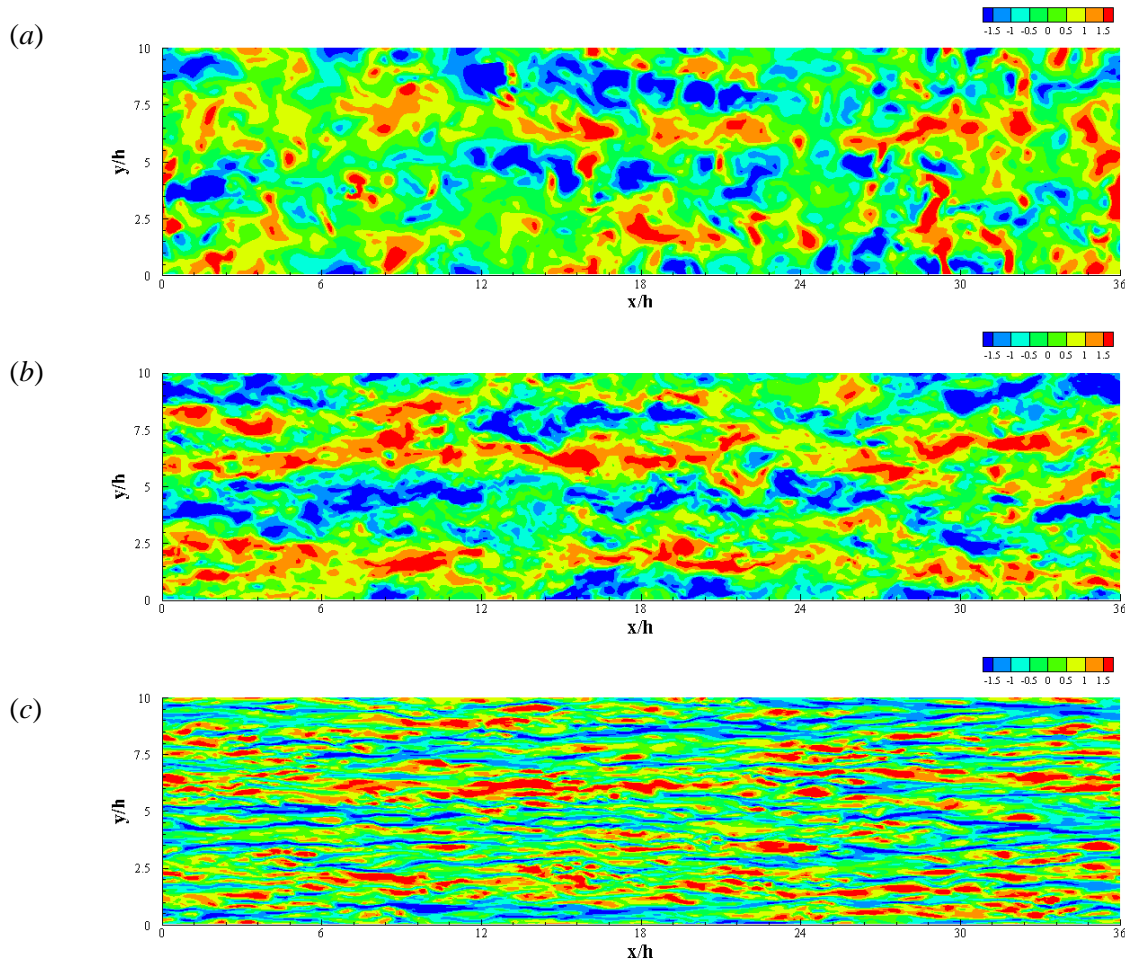

Fig. 9. Contours of normalized instantaneous streamwise velocity fluctuations in the range of $|u/u_{\mathrm{rms}}| < 1.5$ in wall-parallel planes (a) near the moving wall at $z^+ = 350$ ($z/h = 1.94$), (b) at channel center of $z^+ = 180$ ($z/h = 1$) and (c) near the stationary wall at $z^+ = 10$ ($z/h = 0.06$).

To visualize the flow field, Fig. 9 shows the contours of the normalized instantaneous streamwise velocity fluctuation (u/u_{rms}) from the present CP flow. Three xy-planes are chosen, and following the definition sketch in Fig. 1, the planes in Fig. 9 from top to bottom are (a) near the moving wall, (b) the center plane and (c) near the stationary wall, respectively. Planes (a) and (c) are symmetric with respect to the center plane (b) and have a distance of $10\nu/u_\tau$ away from the neighboring wall. Comparing between (a) and (c), it is clear that the flow field is quite different at geometrically symmetric planes, which is in accordance with previous discussions on the statistics of the CP flow. The greatest distinction is the scales of the flow structures in the three wall-parallel planes. The flow structures at the moving wall (a) and the center plane (b) have much larger scales than those close to the stationary wall (c). As shown in Fig. 9 (c) for the near-stationary-wall plane, alternating high- and low-velocity regions are distributed in long streaks

extending in the streamwise direction. These are the well-known near-wall coherent streaky structures also observed in a Poiseuille flow (Kim et al., 1987). These streamwise streaks are associated with the streamwise vortices (ω^+_x in Fig. 8). Away from the stationary wall, with the decreasing of the total shear, the spanwise width of the streaks as well as the spacing between the streaks become increasingly larger, as seen in Fig. 9 (a) and (b). These represent the LSS mentioned before. The velocity contours at the center plane (Fig. 9 (b)) still demonstrate a streamwise streak-like pattern, but near the moving wall they become more cloud-like (Fig. 9 (a)). This observation agrees with Pirozzoli et al. (2011), and seems to indicate the presence of coherent small-scale streaky structures of different sizes up to the center of the channel for the CP flow case, and structures of a larger scale near the moving wall. At this point it is worthwhile to evaluate the wall-normal extension of the different scales and determine if they interact at certain locations.

As has been mentioned in the Methodology, the spanwise spacing of the streamwise structures, which reflects the scale of the structures, can be evaluated by the $\delta y/h$ station of the negative minimum value of the spanwise two-point correlation coefficient R_{uu} defined in Equation 2.3. Recall that Fig. 4 has already demonstrated the spanwise R_{uu} at selected wall-parallel planes. In order to study the complete wall-normal variation of the spanwise spacing of the flow structures, the spanwise R_{uu} is calculated from wall to wall and shown in Fig. 10, in which the magnitude of R_{uu} is reflected by the colors. Fig. 10 (b) shows the 2D projection of Fig. 10 (a) by contours of the R_{uu} values, only for the negative values ($R_{uu} < 0$) for clarity.
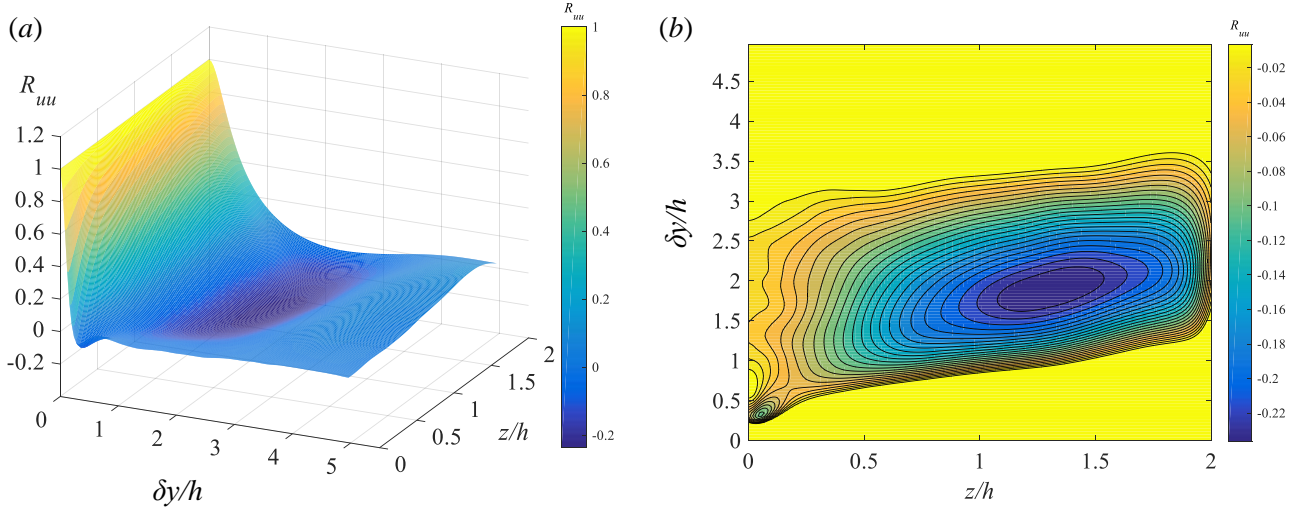

Fig. 10. Distribution of spanwise two-point correlation coefficient $R_{uu}(\delta y)$ in the wall-normal direction. (a) waterfall plot and (b) contour plot showing values of $R_{uu}(\delta y) < 0$.

From Fig. 10 (b), two minima (represented by dark blue color) of R_{uu} can be observed. These two minima are associated with the two most prominent scales, one being the coherent near-wall streaks and the other the LSS. This is reflected by the largely unbalanced surrounding areas of the two minima, indicating greatly distinguishing influencing areas of the two scales. The coherent streaks near the stationary wall correspond to the confined minimum value found at $z^+ \approx 10$ with a spanwise extension of $\delta y/h \approx 0.31$ ($\delta y^+ \approx 55$, at the bottom-left corner of Fig. 10 (b)). The surrounding area of this local minimum value extends to $\delta y/h < 0.65$ ($\delta y^+ < 120$) in spanwise direction and $\delta z/h < 0.2$ ($\delta z^+ < 40$) in wall-normal direction, indicating that the near-stationary-wall structures are relatively small-scale (small δy^+) and their influence is quite local (small δz^+). Structures become much larger in size (both spanwise and wall-normal) while moving away from the stationary wall, i.e. with decreasing mean shear. Also, the influencing area of the small-scale streaky structures is much smaller than that of the LSS. This agrees with Fig. 4, where a sharp negative peak near the stationary wall is observed (Fig. 4 (a)), and the peaks become much less prominent at larger z/h values

(Fig. 4 (b) and (c)). As shown in Fig. 10 (b), the LSS are so large that their influencing area almost covers the whole domain in the wall-normal direction with the center located at $z/h \approx 1.3$ ($z^+ \approx 234$) between the center plane and the moving wall. This is different from the VLS observed in C flows, which have their center located in the channel center plane (see e.g. Tsukahara et al., 2006 and Pirozzoli et al, 2011). Fig. 10 (b) also shows that the spanwise extension of the LSS is also much wider, occupying almost half of the spanwise domain. Being an almost global phenomenon, the outer area of the LSS encloses the area representing the small-scale structures. In general, the spanwise scales of the two different structures near the stationary wall and near the moving wall and the influencing areas of the two scales can be very clearly reflected in Fig. 10 (b).
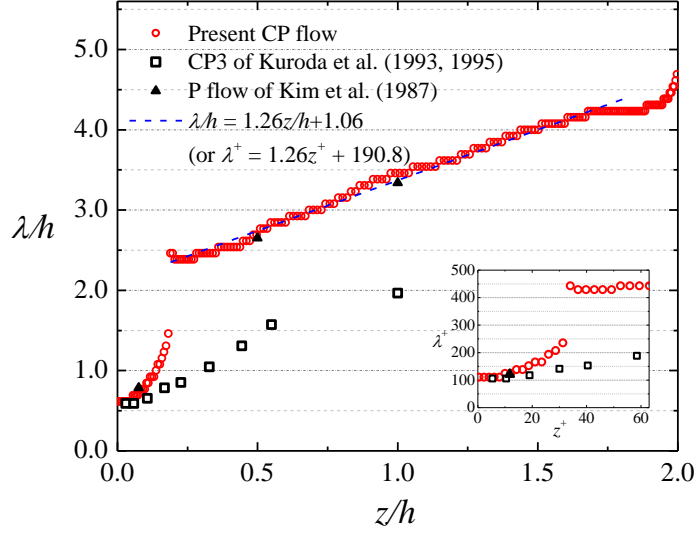

Fig. 11. Distribution of the mean spanwise spacing along the wall-normal direction, estimated from the mean spanwise two-point correlation coefficient $R_{uu}(\delta y)$. The sub-plot shows the zoom-in region near the stationary wall using non-dimensional spacing λ^+ at $Re_{\tau,S} = 180$.

The spanwise spacings of the structures with varying scales obtained from the negative peaks of the spanwise $R_{uu}(\delta y)$ are presented in Fig. 11. The spacings from the CP3 case of Kuroda et al. (1993, 1995) and the P flow case of Kim et al. (1987) are also included for comparison. Only three points were retrieved from Kuroda et al.'s data (recall discussions on Fig. 4), and results for half of the channel height are shown for Kim et al.'s case due to symmetry. It is apparent from Fig. 11 that, when outer scaling is used, Kuroda's data points overlap well with the current results. Compared with the P flow case at the same $Re_{\tau,S}$, the spanwise spacing λ of the shear-less CP flow is larger, and the difference in λ between the P flow and the CP flow increases while moving away from the stationary wall, starting from $z^+ \approx 20$ (see small figure). This confirms again that the LSS observed in the CP flow is a unique feature and is absent in the P flow at $Re_{\tau,S} = 180$. As mentioned before, the normalized wall-normal span (δz^+) of the small-scale near-wall streaks is only about 40 for the current CP flow. Within this z^+ range, the subplot of Fig. 11 shows that λ^+ of CP flow remains almost constant for $z^+ < 10$ but grows slightly for $10 < z^+ < 20$, while the P flow has a constant λ^+ for $z^+ < 20$ and a smaller growth than that of the CP flow for $z^+ > 20$. The larger growth of λ^+ between $10 < z^+ < 35$ for the CP flow indicates the imprinting of the LSS in the buffer region, in consistence with observations from Fig. 10 (b). Within this region, more than one negative peak of spanwise R_{uu} can be observed at different $\delta y/h$ stations, indicating the coexistence of different scales with varying strengths

(figures not shown). All other scales are quite confined (local effects) and much weaker than the two primary scales, and can thus be neglected for the present discussions. Moving away from the stationary wall, the strength of the small-scale near-wall streaks weakens while that of the LSS strengthens. The sudden jump in λ^+ at $z^+ \approx 35$ reflects that the role of the LSS in determining R_{uu} becomes more dominant than that of the small-scale near-wall streaks. The switch of the dominating role and the interaction between the two scales can be observed from Fig. 10 (b). The observation from the inset of Fig. 11 that the spanwise spacing between the near-wall streaks increases much faster in the CP flow than in the P flow indicates the influences of the LSS on the near-wall streaks. The scale of LSS reflected by λ/h continues to grow as the moving wall is nearer. The distribution of the increasing λ/h corresponding to the LSS follows a good linear relation of $\lambda/h = 1.26z/h + 1.06$, as obtained from a linear curve fitting which returns a small standard error of 1% for the slope and 0.6% for the intercept. This linear relation can alternatively be expressed as $\lambda^+ = 1.26z^+ + 190.8$, using wall units at $Re_{\tau,S} = 180$. Contrary to the streaky structures associated with near-wall turbulence, the LSS are unlikely to scale with wall units. The interesting observation that the spacing between the LSS increases almost linearly from about $2.3h$ near the stationary wall to more than $4h$ near the moving wall might be a universal feature of CP flows with zero mean shear. However, the actual slope and intercept of the fitted line are likely to be Reynolds number dependent.

3.3 Kinetic energy of the CP flow

This section will be devoted to energy considerations in the current CP flow. Discussions will be given on the overall kinetic energy and the internal energy conversion between the mean flow and the turbulence. Definition of the total kinetic energy for the mean flow is

$$K = \frac{1}{2}\left(U^2\right) \tag{3.2}$$

and for the turbulence is

$$k = \frac{1}{2}\left(\overline{u_i u_i}\right) = \frac{1}{2}\left(\overline{u^2} + \overline{v^2} + \overline{w^2}\right). \tag{3.3}$$

The wall-normal distribution of K can be easily obtained from the wall-normal profile of U^+ shown in Fig. 6, thus is not presented here. K grows monotonically from the stationary wall to the moving wall and has the largest value at the moving wall with the maximum U^+. The kinetic energy of the mean flow (K) is several orders larger than that of the turbulence (k). The turbulent kinetic energy (TKE) k calculated from Equation 3.3 is plotted in Fig. 12 (a) and the contribution of each velocity component to the total k is shown in Fig. 12 (b). Fig. 12 (a) can be interpreted together with Fig. 7. The energy distribution of the CP flow is unbalanced between the stationary wall and the moving wall, as can be predicted. The value of k is much larger near the stationary wall than near the moving wall, with a peak found at $z^+ \approx 15$ (slightly different from the location of the largest u^+_{rms}). The peak value of k for the CP flow is higher than that of the P flow, which can be explained by recalling the observations from Fig. 7 that all velocity fluctuations of the CP flow are higher than those of the P flow near the stationary wall. Fig. 12 (b) shows that, for both cases, the input from the streamwise velocity fluctuation is the largest across the whole domain, followed by the contribution from the spanwise and wall-normal components. However, close to the moving wall, the percentage of the spanwise contribution increases greatly, although the values of all velocity fluctuations decrease to zero at the wall. Next to the moving wall, the contributions of u^+_{rms} and v^+_{rms} almost equal, unlike near the stationary wall.
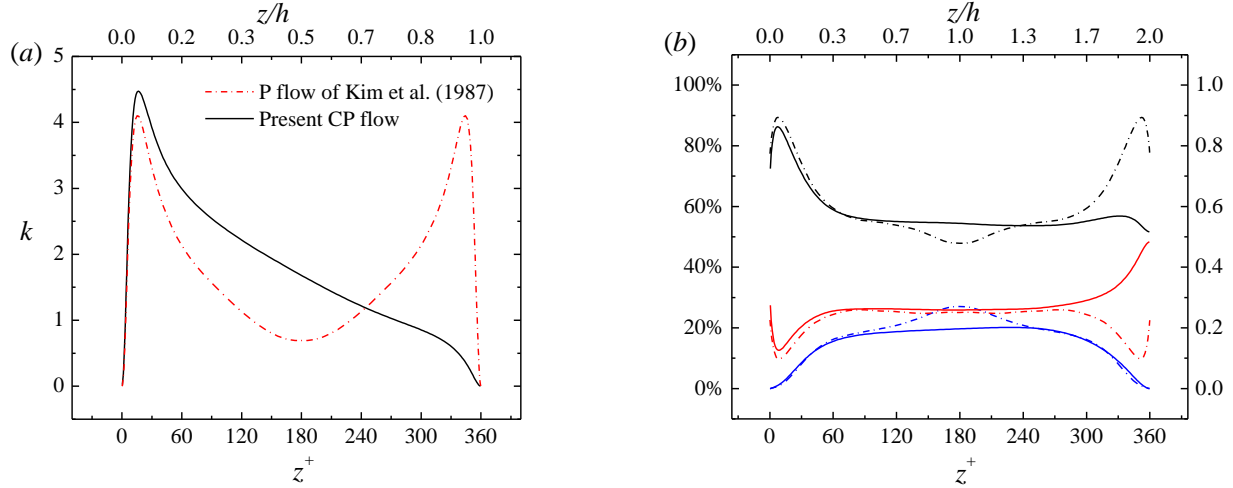
16

Fig. 12. Overall mean turbulent kinetic energy k (TKE) compared to Kim et al. (1987). (a) Comparison of k in the whole domain. Black solid line: the present CP flow; red dashed line: P flow of Kim et al. (1987). (b) Comparison of contribution from the three velocity components across the whole domain (excluding the wall points). Solid lines: present CP flow; dashed lines: Kim et al. (1987)'s results. Black: $u^2_{rms}/2k$; red: $v^2_{rms}/2k$; blue: $w^2_{rms}/2k$.

The energy exchange between the mean flow and the turbulence can be evaluated by studying their energy budgets, respectively. The energy transport equations are derived from the governing Navier-Stokes equations following Tennekes and Lumley (1972). First we will consider the transport equation for the kinetic energy of the mean flow, represented by K. In the present case the mean flow is one-componential and the transport equation of K becomes

$$-\frac{dP}{dx}U + \frac{d}{dz}(\tau U) - \tau\frac{dU}{dz} = -\frac{dP}{dx}U + \frac{d}{dz}(\tau U) - \mu\left(\frac{dU}{dz}\right)^2 + \rho\overline{uw}\frac{dU}{dz} = 0. \qquad 3.4$$

The overall energy conversion can be obtained by integration of Equations 3.4 for the whole domain from wall to wall, i.e. $z = 0$ to $2h$. Note that, theoretically, term $\int_0^{2h}\frac{d}{dz}(\tau U)dz$ from Equation 3.4 is essentially zero since $U = 0$ on the stationary wall at $z/h = 0$ and $\tau_M = 0$ on the moving wall at $z/h = 2$. This means the moving wall at $z/h = 2$ does not contribute any kinetic energy to the flow field, as a result of the zero mean shear. This is one key feature of the current shear-less CP flow. The integration equation then becomes

$$\underbrace{-\frac{dP}{dx}\int_0^{2h}Udz}_{A} \underbrace{-\int_0^{2h}\mu\left(\frac{dU}{dz}\right)^2 dz}_{B} + \underbrace{\int_0^{2h}\rho\overline{uw}\frac{dU}{dz}dz}_{C} = 0. \qquad 3.5$$

The resulting non-zero terms in Equation 3.5 are evaluated individually. Term A represents the total supply of mechanical energy to the mean flow, caused by the pressure gradient which drives the fluid in the positive x-direction. Term B represents the total deformation work by the viscous shear stress and is always negative. This term indicates the loss of mean-flow kinetic energy K by means of viscous dissipation. The last term (C) represents the total deformation work by Reynolds shear stress. This term is always negative, provided that $\overline{uw} \leq 0$ and $dU/dz \geq 0$ everywhere in the flow, and is therefore a loss of K. As will be shown later, the lost energy is converted into mean turbulent kinetic energy k. The values for each integrated term, after normalized by $\rho u^3_{\tau,S}$, are calculated from the present CP flow database:

$$\text{Term } A: -\frac{1}{2Re_{\tau,S}}\int_0^{2h^+}U^+dz^+ = 17.06;$$

17

$$\text{Term } B: \; -\int_0^{2h^+} \left(\frac{\mathrm{d}U^+}{\mathrm{d}z^+}\right)^2 \mathrm{d}z^+ = -8.54 \;;$$

$$\text{Term } C: \int_0^{2h^+} \overline{u^+ w^+}\, \frac{\mathrm{d}U^+}{\mathrm{d}z^+}\, \mathrm{d}z^+ = -7.99.$$

This indicates that the total energy input provided by term A is almost evenly distributed between the viscous stress deformation work (term B) and the turbulent stress deformation work (term C). Note that the sum of the three terms is 0.53. This small deviation from zero is caused by the fact that, for the DNS results of the current CP flow, the total shear stress at the grid points located on the moving wall boundary is not exactly zero (although close enough to have a low mean value of $|\tau_\mathrm{M}/\rho u_{\tau,\mathrm{S}}^2| \approx 0.003$). Due to the relatively large mean velocity at the moving wall ($U^+_\mathrm{wall} = 20$), the integrated value of the term $\frac{\mathrm{d}}{\mathrm{d}z}(\tau U)$ from Equation 3.4 is thus not totally negligible, which results in the total sum of the calculated terms in Equation 3.5 to be slightly different from zero.

The three terms for the P flow of Kim et al. (1987) are also calculated to compare with the current CP flow. Although the pressure gradient is the same for the two flow cases, term A for the CP flow is larger than the same term for the P flow (17.06 vs 15.80), indicating that although the wall motion does not provide extra mechanical energy for the CP flow, it increases the energy input by the driving pressure gradient to the mean flow. As for the comparison of the loss terms B and C between the two flow cases, term B for the CP flow is smaller (-8.54 vs -9.25) while term C for the CP flow is larger (-7.99 vs -6.18), meaning less viscous stress deformation work and more turbulence stress deformation work, under the influences of the shear-less moving wall. The loss term C changes its sign and thus serves as a gain term in the energy transport equation for k, representing the kinetic energy obtained from the mean flow to the turbulence. Therefore, the increase in term C observed for the CP flow corresponds to a higher k compared to the P flow, in accordance with Fig. 12 (a).

For the turbulence, the energy transport equation for k can be written as the following:

$$\underbrace{-\rho\overline{uw}\frac{\mathrm{d}U}{\mathrm{d}z}}_{P} \underbrace{-\rho\frac{\mathrm{d}}{\mathrm{d}z}\overline{pw}}_{D_\mathrm{turb,p}} \underbrace{-\rho\frac{\mathrm{d}}{\mathrm{d}z}\left(\frac{1}{2}\overline{u_i u_i w}\right)}_{D_\mathrm{turb,w}} + \underbrace{\mu\frac{\mathrm{d}^2 k}{\mathrm{d}z^2}}_{D_\mathrm{visc}} \underbrace{-\mu\overline{\frac{\partial u_i}{\partial x_j}\frac{\partial u_i}{\partial x_j}}}_{\varepsilon} = 0, \tag{3.6}$$

where P is the production term; $D_\mathrm{turb,p}$ and $D_\mathrm{turb,w}$ represent the turbulent diffusion terms associated with pressure fluctuations and velocity fluctuations, respectively; D_visc indicates the viscous diffusion; and ε is the energy dissipation rate. The expressions from Equation 3.6 are the same as those used by Mansour et al. (1988), Komminaho et al. (1996), and Pirozzoli et al. (2011), etc.

It is seen that the production term P appears both in Equation 3.4 for the mean-flow K equation (corresponding to term C in Equation 3.5) and in Equation 3.6 for the turbulence k, but with an opposite sign. As mentioned before, P is negative and is a loss term in the K equation, while in transport equation for k it becomes a gain term to the turbulence. Komminaho et al. (1996) presented a model to predict the wall-normal location and the magnitude of the maximum P, which assumes that U^+ in the range from the wall to the buffer layer can be modeled as

$$U^+ = 13.6\times\tanh\left(\frac{z^+}{13.6}\right). \tag{3.7}$$

Following this U^+ model and considering Equation 3.6, the normalized production term for the present CP flow can then be written as

$$P^+ = \frac{\mathrm{d}U^+}{\mathrm{d}z^+}\left(1 - \frac{\mathrm{d}U^+}{\mathrm{d}z^+} - \frac{z^+}{2h^+}\right). \tag{3.8}$$

The maximum P^+ predicted by Equation 3.8 is 0.231 at $z^+ \approx 12$. The results given by Equation 3.8 shows that the production for the CP flow is slightly larger than for the P flow of Kim et al. (1987), but the corresponding z^+ is the same for both cases. This matches well with the present DNS data for the CP flow, which is shown in Fig. 13 (same as the CP3 case of Kuroda et al., 1993, 1995).
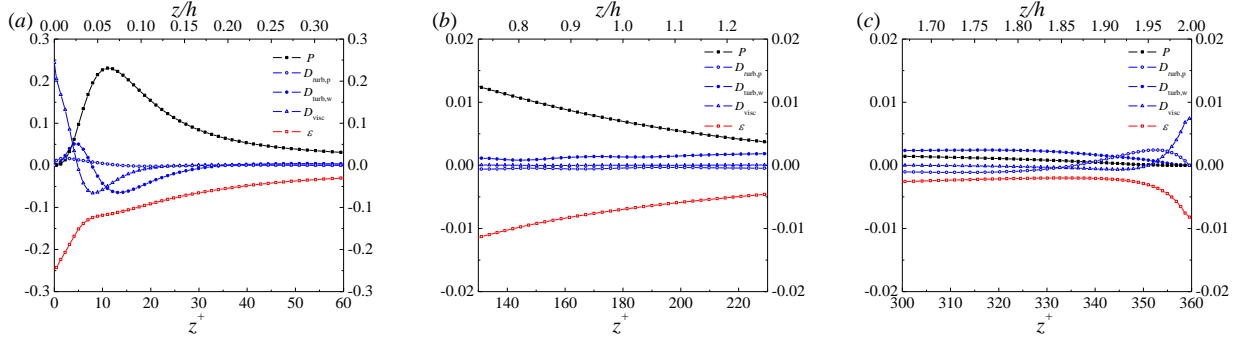

Fig. 13. The wall-normal distribution of budgets of the mean turbulent kinetic energy k near (a) the stationary wall from $z^+ = 0$ to 60, (b) the center region from $z^+ = 130$ to 230 and (c) the moving wall from $z^+ = 300$ to 360. Note the scale of the vertical axis in (a) is an order-of-magnitude larger than in (b) and (c).

The terms in Equation 3.6 are plotted in Fig. 13. In the near-stationary-wall region (Fig. 13 (a)), the curves have similar trends to those in the P flow case (the latter not shown). Attaching the stationary wall, the dissipation term ε and the viscous diffusion term D_{visc} have the largest magnitudes and balance each other, while all the other terms go to zero. Slightly above the stationary wall, the magnitudes of ε and D_{visc} begin to decrease, while the other terms begin to increase. First an almost negligible peak of $D_{\text{turb,p}}$ is found very close to the stationary wall. Next a relatively small peak of $D_{\text{turb,w}}$ occurs before the term decreases to negative values together with D_{visc}. The production term P has the highest peak among all terms, which is found at $z^+ \approx 12$, as mentioned before. At this z^+ all other terms are negative and act as loss terms, balanced by the only gain term P.

The magnitudes of all terms have a general decreasing trend leaving the stationary wall and approaching the moving wall (Fig. 13 (b)). In the center region, all terms are relatively small. The production term P is still the dominant gain term to balance the dominant dissipation term ε, while $D_{\text{turb,w}}$ also serves as a minor gain term. The magnitudes of P and ε continue to decrease towards the moving wall. As shown in Fig. 13 (c), for $z^+ < 340$ in the proximity of the moving wall, the production term P reduces to be the secondary gain term, and the turbulent diffusion term $D_{\text{turb,w}}$ serves as the largest gain term. The dominating role played by $D_{\text{turb,w}}$ as a gain term will be further evaluated later. Both $D_{\text{turb,w}}$ and P reduce to zero at the moving wall, while the role to balance the dissipation term is exchanged between different terms. At $z^+ > 330$, the pressure diffusion term $D_{\text{turb,p}}$ begins to increase and becomes positive, changing from a loss term to a gain term. It becomes the main term to balance the dissipation near the moving wall, before decreases to zero at the wall, forming a peak. Note that this peak of $D_{\text{turb,p}}$ (in Fig. 13 (c)) is much smaller than the peak of $D_{\text{turb,p}}$ near the stationary wall (in Fig. 13 (a)). Slightly after the peak of $D_{\text{turb,p}}$ and further nearer the moving wall, the viscous diffusion term D_{visc} increases and balances the increasing $|\varepsilon|$ for $z^+ > 350$. Unlike near the stationary wall, all terms at the moving wall are much smaller. This indicates that the generation and conversion of the turbulent kinetic energy k is local and the strongest near the stationary wall, associated with the relatively small-scale structures, while the energy conversion activity is much reduced near the moving wall where it is mainly realized through the turbulent diffusion terms. The LSS, however, play an important role in the overall energy transfer throughout the whole domain thanks to their global scales.

To further explore the leading role of $D_{turb,w}$ near the moving wall, Fig. 14 shows the different third-moments $\overline{q^2 w} = \overline{u^2 w} + \overline{w^2 w} + \overline{w^3}$ that contribute to the turbulence-driven diffusive transport across the channel. First of all, one can observe that $\overline{q^2 w}$ decreases monotonically all the way from $z^+ \approx 30$ to the moving wall, thereby gives rise to a flux of k from the zone near the stationary wall where a substantial mean-shear production P occurs, to the moving wall where P is negligibly small. The positive value of $\overline{q^2 w}$ is at least qualitatively consistent with the frequently adopted gradient-type diffusion hypothesis $\overline{q^2 w} \propto -dk/dz$ (see Fig. 12 (a)). Furthermore, it is noteworthy that, while $\overline{u^2 w}$ dominates the turbulent diffusion in the vicinity of the stationary wall, $\overline{w^3}$ becomes equally important near the moving wall where $D_{turb,w}$ becomes the primary source of turbulent energy. Thus, contrary to the P flow, wall-normal velocity fluctuations w correlate equally well with u^2 and w^2. This anomalous diffusion is likely to be associated with the LSS which are essentially non-existing in P flows at this fairly low Reynolds number.
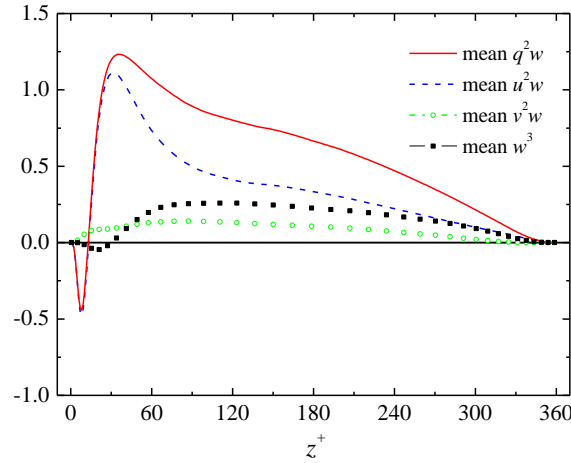

Fig. 14. Distribution of third-order moments across the CP flow.

Integration of Equation 3.6 for the overall k conversion from wall to wall gives

$$-\int_0^{2h} \rho \overline{uw} \frac{dU}{dz} dz - \int_0^{2h} \rho \frac{d}{dz} \overline{pw} dz - \int_0^{2h} \rho \frac{d}{dz} \left(\frac{1}{2} \overline{u_i u_i w} \right) dz + \int_0^{2h} \mu \frac{d^2 k}{dz^2} dz - \int_0^{2h} \mu \overline{\frac{\partial u_i}{\partial x_j} \frac{\partial u_i}{\partial x_j}} dz = 0. \qquad 3.9$$

Due to the no-slip condition at the walls, all velocity fluctuations go to zero, therefore the terms $\int_0^{2h} \rho \frac{d}{dz} \overline{pw} dz$ for $D_{turb,p}$ and $\int_0^{2h} \rho \frac{d}{dz} \left(\frac{1}{2} \overline{u_i u_i w} \right) dz$ for $D_{turb,w}$ are also zero. To validate this point, the diffusion terms normalized by $\rho u^3_{\tau,S}$ are calculated from the current DNS results, and the values are $-\int_0^{2h^+} \frac{d}{dz^+} \overline{p^+ w^+} dz^+ = 6.5 \times 10^{-3}$ and $-\int_0^{2h^+} \frac{d}{dz^+} \left(\frac{1}{2} \overline{u_i^+ u_i^+ w^+} \right) dz^+ = 3.63 \times 10^{-4}$. This proves the negligibility of these two diffusion terms. Hence Equation 3.9 simply becomes

$$-\int_0^{2h} \rho \overline{uw} \frac{dU}{dz} dz + \int_0^{2h} \mu \frac{d^2 k}{dz^2} dz - \int_0^{2h} \varepsilon \, dz = 0. \qquad 3.10$$

$$\underbrace{\qquad\qquad}_{C'} \qquad \underbrace{\qquad}_{B'} \underbrace{\qquad}_{D'}$$

20

In this equation, term *C'* is the total kinetic energy transferred from the mean flow to the turbulent flow and the calculated value for this term after normalization is $-\int_0^{2h^+} \overline{u^+w^+} \frac{dU^+}{dz^+} dz^+ = 7.99$, in consistence with term *C* calculated from Equation 3.5; term *B'*, normalized as $Re_{\tau,S}\int_0^{2h^+} \frac{d^2k^+}{dz^{+2}} dz^+$, is the total energy distributed by viscous diffusion from wall to wall, and has a negligible value of 0.06; the last term, term *D'*, the total energy dissipated by the turbulence, almost equals term *C'* with a value of $-Re_{\tau,S}\int_0^{2h^+} \varepsilon^+ dz^+ \approx -7.26$. . It is noted that, the value of term *B'* in Equation 3.10 is the overall difference between the complete form of viscous diffusion $(Re_{\tau,S}\int_0^{2h^+} \frac{d}{dz^+}\left[\overline{u_i^+(\frac{\partial u_i^+}{\partial z^+}+\frac{\partial w^+}{\partial x_i^+})}\right])$ and the current one used here; at the same time, it also equals the difference between the complete thermodynamic expression for the viscous dissipation term $(Re\int_0^{2h^+} \frac{1}{2}\overline{\left(\frac{\partial u_i^+}{\partial x_j^+}+\frac{\partial u_j^+}{\partial x_i^+}\right)\left(\frac{\partial u_i^+}{\partial x_j^+}+\frac{\partial u_j^+}{\partial x_i^+}\right)})$ and the current one used here. The current result shows that the difference between the different expressions is within 1% and is thus negligible, in consistence with the previous discussions on this issue (Bradshaw and Perot, 1993).

4   Conclusions

This paper describes a DNS study of a particular Couette-Poiseuille flow with the special consideration that the total shear stress monotonically decreases and reaches zero at one wall. The shear-less CP flow was obtained by prescribing a relative velocity at the wall, in addition to a driving pressure gradient in the streamwise direction. The current study achieved a negligible total shear of $|\tau_M/\rho u_{\tau,S}^2| \approx 0.003$ at the moving wall. The Reynolds number is $Re_{\tau,S} = 180$ based on $u_{\tau,S}$ (the friction velocity at the stationary wall) and $Re_{\tau,M} = 9.8$ based on $u_{\tau,M}$ (the friction velocity at the moving wall). First the results obtained for the present CP flow are validated against Kuroda et al. (1993, 1995)'s similar shear-free case at a comparable Reynolds number of $Re_{\tau,S} = 154$. We succeeded to produce a flow field for which the mean shear stress at the moving wall was much closer to zero than that achieved by Kuroda et al. (1993, 1995). Moreover, a finer grid resolution and a longer and wider computational domain were used for the present computations. Then the influences of prescribing a shear-less moving wall are discussed in mainly three aspects, including the primary flow statistics, the different scales of the flow structures, and the energy considerations. Extensive comparison to the Poiseuille flow case of Kim et al. (1987) at the same $Re_{\tau,S}$ is performed, by which the unique features of the present CP flow are reflected. The main findings of the present study are summarized below.

- Most primary statistics, including the shear stresses, the mean streamwise velocity, the turbulent intensities and the fluctuating vorticities, are all compared to the P flow case. The asymmetric shear condition in the whole flow field due to the additional freedom at one wall results in the asymmetricity of all these statistical quantities. Near the stationary wall, the flow features are similar to those of Kim et al. (1987)'s P flow, but with slight differences caused by the imprinting of the moving wall effects. Away from the stationary wall and approaching the moving wall, the effects of the latter become more apparent. Specifically, differences in the primary statistics between the current CP flow data and the P flow data are observed: a higher total stress in the center region due to a higher turbulent stress; a much longer logarithmic region of the mean streamwise velocity with lower values of κ and B from the log-scale approximation; larger turbulent intensities near the stationary wall but smaller near the moving wall. The main interest lies in the moving wall region. Here the total stress falls to zero, and the mean velocity reaches its maximum value following the

wall velocity, while all turbulent intensities reduce to zero due to no-slip and impermeability of the wall. All the vorticity components decrease, until very close to the moving wall where they increase slightly as a result of the no-slip boundary condition. No streamwise vorticities are formed and the vorticity have smaller values at the moving wall.

- The different scales of flow structures formed in the shear-less CP flow are explored by means of spanwise two-point correlation coefficient of the streamwise velocity fluctuations. Two different dominating scales are found at different wall-normal locations. One is the near-wall coherent streaks formed in the buffer layer next to a stationary wall. The coherent streaks are local, i.e. extend up to $z^+ \approx 35$; they are also small-scale, with an increasing spanwise spacing of 100 to 250 wall units. This increase of spanwise spacing is faster than in the P flow case due to the imprinting of the Large-Scale-Structures (LSS), which are absent in the P flow at this low $Re_{\tau,S}$. The LSS have their center located near the channel center region, and have an almost global effect: the LSS extend from the buffer layer near the stationary wall, where their influences on the small-scale streaks begin to show, to very close to the moving wall. With the decrease of the total shear, the LSS tend to increase in spanwise spacing and change from streak-like to cloud-like. The spanwise extension of the LSS increases from $2.3h$ to $4.2h$ following a linear relation over a large region of the domain, and increases more sharply very close to the moving wall to about $4.5h$.

- The overall kinetic energy of the mean flow (K) is much larger than that of the turbulence (k), and the distributions of both K and k are different in the current CP flow compared to a P flow. The present CP flow obtains its energy input only from the pressure gradient, and there is no energy input by the moving wall due to zero mean shear. This point is clear by looking at the internal energy conversion of both the mean flow and the turbulence, from which it is found that the kinetic energy is mainly generated near the stationary wall and transferred to the moving wall region, while the latter provides no energy contribution to the flow field. Half of the energy input provided by the streamwise pressure gradient is converted into the turbulence kinetic energy and the other half is lost due to viscous dissipation. Although the wall motion provides no extra energy to the CP flow, it enhances the energy input from the driving pressure gradient to the mean flow field, and increases the production term near the stationary wall, compared to that of a P flow. The terms in the k transport equation behave quite differently near the two walls. In addition to no turbulence production near the moving wall, the magnitude for each term is much smaller compared to the near-stationary-wall region, and the gain terms balancing the dissipation are quite different near the two walls. The LSS play an important role in transferring energy through their global effects.

The main contribution of the present work includes, 1) presented detailed data on this particular CP flow field from the stationary wall to the zero-mean-shear moving wall; 2) investigated the different scales of the flow structures formed in this particular flow; 3) described the influence of the moving wall on the coherent turbulent structures near the stationary wall; and 4) studied the energy conversion for the first time in literature for this particular CP flow. Such information serves to further our understanding of wall-bounded turbulence in general.

Acknowledgements

References

Alfredsson, P.H., Johansson, A.V., 1984. On the detection of turbulence-generating events. J. Fluid Mech. 139, 325–345.

Avsarkisov, V., Hoyas, S., Oberlack, M., García-Galache, J.P., 2014. Turbulent plane Couette flow at moderately high Reynolds number. J. Fluid Mech. 751, R1-R9.

Balakumar, B.J., Adrian, R.J., 2007. Large- and very-large-scale motions in channel and boundary-layer flows. Phil. Trans. R. Soc. A., 365, 665-681.

Bech, K.H., Andersson, H.I., 1996. Structure of Reynolds shear stress in the central region of plane Couette flow. Fluid Dyn. Res. 18, 65–79.

Bech, K.H., Andersson, H.I., 1994. Very-large-scale structures in DNS. In: Direct and Large-Eddy Simulation I. Volume 26 of the series Fluid Mechanics and Its Applications. Springer Netherlands, 13–24.

Bech, K.H., Tillmark, N., Alfredsson, P.H., Andersson, H.I., 1995. An investigation of turbulent plane Couette flow at low Reynolds numbers. J. Fluid Mech. 286, 291–325.

Bradshaw, P., Perot, J.B., 1993. A note on turbulent energy dissipation in the viscous wall region. Phys. Fluids A. 5, 3305–3306.

Coleman, G.N., Spalart, P.R., 2015. Direct numerical simulation of turbulent Couette-Poiseuille flow with zero skin friction. 15th Eur. Turbul. Conf. 25-28 August, 2015, Delft, Netherlands.

Coleman, G.N., Pirozzoli, S., Quadrio, M., Spalart, P.R., 2016. Direct numerical simulation and theory of a wall-bounded flow with zero skin friction. In: 11th International ERCOFTAC Symposium on Engineering Turbulence Modelling and Measurements. 21-23 September, 2016, Palermo, Italy.

Gai, J., Xia, Z.H., Qing-Dong, C., 2015. Effects of the computational domain on the secondary flow in turbulent channel flow. Chin. Phys. B, 24, 104701.

Gillissen, J.J.J., Boersma, B.J., Mortensen, P.H., Andersson, H.I., 2007. On the performance of the moment approximation for the numerical computation of fiber stress in turbulent channel flow. Phys. Fluids. 19, 035102.

Hamilton, J.M., Kim, J., Waleffe, F., 1995. Regeneration mechanisms of near-wall turbulence structures. J. Fluid Mech. 287, 317–348.

Holstad, A., Johansson, P.S., Andersson, H.I., Pettersen, B., 2006. On the influence of domain size on POD modes in turbulent plane Couette flow. In: Direct and Large-Eddy Simulation VI, 763-770, Springer, Dordrecht.

Holstad, A., Andersson, H.I., Pettersen, B., 2009. Turbulence in a three-dimensional wall-bounded shear flow. Int. J. Numer. Methods Fluids 62, 875–905.

Jeong, J., Hussian, F., Schoppa, W., Kim, J., 1997. Coherent structures near the wall in a turbulent channel flow. J. Fluid Mech. 332, 185–214.

Jiménez, J., Pinelli, A., 2002. Coherent structure generation in near-wall turbulence. J. Fluid Mech. 453, 57–108.

Kawahara, G., Kida, S., 2001. Periodic motion embedded in plane Couette turbulence: regeneration cycle and burst. J. Fluid Mech. 449, 291–300.

Kim, J., Moin, P., Moser, R., 1987. Turbulence statistics in fully developed channel flow at low Reynolds number. J. Fluid Mech. 177, 133–166.

Komminaho, J., Lundbladh, A., Johansson, A. V., 1996. Very large structures in plane turbulent Couette flow. J. Fluid Mech. 320, 259–285.

Kuroda, A., Kasagi, N., Hirata, M., 1993. Direct numerical simulation of turbulent plane Couette-Poiseuille flows: effect of mean shear on the near wall turbulence structures. In Proc. 9th Symp. Turbulent Shear Flows, Tokyo, 1, 8.4.1–8.4.6.

Kuroda, A., Kasagi, N., Hirata, M., 1995. Direct numerical simulation of turbulent plane Couette-Poiseuille flows: effect of mean shear rate on the near wall turbulence structures. Turbulent Shear Flows 9, Springer, 241–257.

Lam, K., Banerjee, S., 1992. On the condition of streak formation in a bounded turbulent flow. Phys. Fluids A. 4, 306–320.

Lee, M.J., Kim, J., Moin, P., 1990. Structure of turbulence at high shear rate. J. Fluid Mech. 216, 561–583.

Lee, M.J., Kim, J. 1991. The structure of turbulence in a simulated plane Couette flow. In Proc. 8th Symp. Turbulent Shear Flows, Munich, 5.3.1–5.3.6.

Mansour, N.N., Kim, J., Moin, P., 1988. Reynolds-stress and dissipation-rate budgets in a turbulent channel flow. J. Fluid Mech. 194, 15–44.

Mortensen P.H., Andersson, H.I., Gillissen, J.J.J., Boersma B.J., 2008. Dynamics of prolate ellipsoidal particles in a turbulenct channel flow. Phys. Fluids 20, 093302.

Orlandi, P., Jiménez, J., 1994. On the generation of turbulent wall friction. Phys. Fluids 6, 634–641.

Pirozzoli, S., Bernardini, M., Orlandi, P., 2011. Large-scale motions and inner/outer layer interactions in turbulent Couette–Poiseuille flows. J. Fluid Mech. 680, 534–563.

Robinson, S.K., 1991. Coherent motions in the turbulent boundary layer. Annu. Rev. Fluid Mech 23, 601–639.

Rogers, M.M., Moin, P., 1987. The structure of the vorticity field in homogeneous turbulent flows. J. Fluid Mech. 176, 33–66.

Tennekes, H., Lumley, J.L., 1972. A first course in turbulence. The MIT Press.

Tsukahara, T., Kawamura, H., Shingai, K., 2006. DNS of turbulent Couette flow with emphasis on the large-scale structure in the core region. J. Turbul. 7, N19.

Waleffe, F., 2001. Exact coherent structures in channel flow. J. Fluid Mech. 435, 93–102.

Wallace, J.M., Eckelmann, H., Brodkey, R.S., 1972. The wall region in turbulent shear flow. J. Fluid Mech. 54, 39–48.

Zhao, L., Andersson, H.I., Gillissen, J.J.J., 2013. Interphasial energy transfer and particle dissipation in particle-laden wall turbulence. J. Fluid Mech. 715, 32–59.

Zhou, J., Adrian, R.J., Balachandar, S., 1996. Autogeneration of near wall vortical structures in channel flow. Phys. Fluids. 8, 288–3194.